Characterizing the Location and Extent of Myocardial Infarctions With Inverse ECG Modeling and Spatiotemporal Regularization

Bing Yao, Rui Zhu, and Hui Yang, *Senior Member, IEEE*

***Abstract*—Myocardial infarction (MI) is among the leading causes of death in the United States. It is imperative to identify and characterize MIs for timely delivery of life-saving medical interventions. Cardiac electrical activity propagates in space and evolves over time. Traditional works focus on the analysis of time-domain ECG (e.g., 12-lead ECG) on the body surface for the detection of MIs, but tend to overlook spatiotemporal dynamics in the heart. Body surface potential mappings (BSPMs) provide high-resolution distribution of electric potentials over the entire torso, and therefore provide richer information than 12-lead ECG. However, BSPM are available on the body surface. Clinicians are in need of a closer look of the electric potentials in the heart to investigate cardiac pathology and optimize treatment strategies. In this paper, we applied the method of spatiotemporal inverse ECG (ST-iECG) modeling to map electrical potentials from the body surface to the heart, and then characterize the location and extent of MIs by investigating the reconstructed heart-surface electrograms. First, we investigate the impact of mesh resolution on the inverse ECG modeling. Second, we solve the inverse ECG problem and reconstruct heart-surface electrograms using the ST-iECG model. Finally, we propose a wavelet-clustering method to investigate the pathological behaviors of heart-surface electrograms, and thereby characterize the extent and location of MIs. The proposed methodology is evaluated and validated with real data of MIs from human subjects. Experimental results show that negative QRS waves in heart-surface electrograms indicate potential regions of MI, and the proposed ST-iECG model yields superior characterization results of MIs on the heart surface over existing methods.**

***Index Terms*—Inverse ECG problem, myocardial infarction, spatiotemporal regularization, wavelet clustering.**

I. Introduction

MYOCARDIAL infarction (MI), commonly known as heart attack, is among the leading causes of death throughout the world. It is shown that approximately every 40 seconds, an American will suffer a heart attack [1]. MI occurs due to the blockage of coronary arteries. This will significantly decrease or stop the blood flow or oxygen supply to the heart, thereby damaging the heart muscle and triggering the heart attack. According to the American Heart Association, heart disease accounts for approximately 1 in 7 deaths in 2016, and there are about 790,000 people experience heart attacks annually in the United States [1]. MI is among the most expensive diseases for clinical diagnosis, medical treatment, and follow-up care. The economic costs of heart diseases are estimated to be around $1,044 billion by 2030 [1]. The effective time window for MI treatments is within one hour from the onset of symptoms. Therefore, it is imperative to characterize and identify MIs in the early stage for timely delivery of optimal medical interventions and the improvement of heart health.

There are two categories of tests commonly used in clinical practice for the MI identification, namely structure imaging or functional sensing. Structure imaging is essentially frozen screenshots of heart structures. For example, computed tomography (CT) helps examine the inside structure of the heart and identify tissue damages. Magnetic resonance imaging (MRI) utilizes the magnetic fields to get images of the heart. Most of them are expensive tests conducted in a short period of time and are not always readily available. Even if routine examinations are performed multiple times each day, the intermittence still fails to detect life-threatening cardiac events [2]. Functional sensing captures a wealth of information pertinent to dynamic changes in cardiac conditions, e.g., electrocardiogram (ECG) signals. Cardiac dynamics over time are essential to monitor the progression of disease processes.

The 12-lead ECG is widely used for the identification of MIs by checking abnormalities in ECG wave deflections, e.g., significant Q waves, ST depression/elevation, or inverted T-waves. It may be noted that cardiac electrical activity propagates in space and evolves in time. One lead ECG captures 1-dimensional views of such space-time cardiac electrical activity. The 12-lead ECG systems provide 12-directional views of such space-time dynamics [3]. Most existing works [4], [5] focus on the analysis of time-domain ECG signals on the body surface for the detection of ECG wave deflections (i.e., P, QRS, T waves) on the body surface but tend to overlook spatiotemporal dynamics in the heart [4]–[6]. Time-domain ECG is a projected view of spatiotemporal cardiac electrical activity that diminishes important spatial information pertinent to heart diseases (e.g., myocardial infarction). Because distributed sensors at various locations

Manuscript received May 10, 2017; revised September 20, 2017 and October 28, 2017; accepted October 29, 2017. This work was supported in part by the National Science Foundation (CMMI-1646660) and in part by Harold and Inge Marcus Career Professorship (HY). *(Corresponding author: Hui Yang.)*

The authors are with the Complex System Monitoring, Modeling and Analysis Laboratory, The Pennsylvania State University, University Park, PA 16802 USA (e-mail: BZY111@psu.edu; RZZ45@psu.edu; huy25@psu.edu).

Digital Object Identifier 10.1109/JBHI.2017.2768534

on the body surface respond to changes of heart conditions differently, body surface potential mapping (BSPM) employs hundreds of sensors to achieve high-resolution ECG sensing. High-resolution ECG images from BSPM facilitate the reconstruction of spatiotemporal distribution of electric potentials over the entire torso, and therefore provide richer information than 12-lead ECG for clinical decision making [7], [8].

However, ECG images provide the distribution of electrical potentials on the body surface. Clinicians call for the estimation of heart-surface potentials to delineate pathological changes in the heart (e.g., infarct tissues). This is also called inverse ECG problem. Note that spatiotemporal ECG data and complex torso-heart geometries pose significant challenges on analytical modeling of the relationship between body-surface potentials $\boldsymbol{\phi}_B(t)$ and heart-surface potentials $\boldsymbol{\phi}_H(t)$. The high-dimensional predictive model, $\boldsymbol{\phi}_B(t) = \boldsymbol{R}_{BH}\boldsymbol{\phi}_H(t) + \boldsymbol{\epsilon}$, is generally ill-conditioned. The transfer matrix $\boldsymbol{R}_{BH}$ is derived based on torso-heart geometries and electromagnetic theory, but physics-based models do not account for real-world uncertainties (i.e., approximation errors and measurement noises), and therefore do not always match satisfactorily with data from real-world experiments. Our previous investigation developed a new methodology of spatiotemporal regularization (STRE) to solve inverse ECG problems, see details in [9]. This approach leverages ECG data to improve the spatial and temporal regularity of the solutions, thereby making more accurate predictions (closer to reality). Note that the STRE model involves both the spatial and temporal regularization terms, and is difficult to be solved analytically. We developed an iterative algorithm of dipole multiplicative update, inspired by the dipole assumptions in electrodynamic physics, to solve spatiotemporal regularization problems.

In this paper, we further investigate the application of the STRE model to reconstruct heart-surface potentials from BSPMs for MI characterization. Also, we develop a wavelet-clustering method to cluster time series of electrical potentials on the heart surface and thereby characterize the extent and location of the MIs. Specifically, our contributions in the present investigation are as follows:

1) *Wavelet clustering of heart-surface electrograms to differentiate healthy and infarcted regions:* It is common to identify and characterize MIs by checking abnormalities of time-domain ECGs on the *body surface* (i.e., significant Q waves, ST depression/elevation, and inverted T waves). However, little has been done to study pathological behaviors of *heart-surface* electrograms in the time-frequency domain. We solve the inverse ECG problem using the STRE model and propose a wavelet-clustering method of heart electrograms to differentiate healthy and infarcted patterns. Different frequency bands of heart-surface electrograms are studied. Experimental results show approximation bands provide better characterization results than detailed bands. (See details in the experimental results.)

2) *Case studies on ECG images from human subjects:* First, we performed wavelet-clustering of the electrograms on the heart surface for two training cases. We studied different segments of heart-surface ECGs, including the entire ECG cycle, P wave, QRS wave, and T wave. Experimental results show that QRS clustering yields the best characterization of MIs based on the MRI images. Second, we validated the characterization results with the other two test cases, and found consistent results that the cluster of negative QRS waves on the heart surface indicates potential infarction areas. The characterization results by the proposed methodology are further benchmarked with golden standards provided by Gadolinium-enhanced transaxial MRI (GE-MRI) images.

The rest of this paper is organized as follows: Section II introduces the research background of existing MI characterization methods and inverse ECG problems. Section III presents the research methodology of spatiotemporal inverse ECG model and wavelet clustering. Section IV describes the experimental design and results. Section V concludes the present investigation.

II. Research Background

A. Characterizing MIs From BSPMs

BSPM employs hundreds of electrodes on the body surface and records the spatiotemporal distribution of electric potentials over the entire torso. Many previous studies characterized the size and location of MIs by investigating BSPMs. Simelius *et al.* [10] proposed the use of self-organizing maps to analyze and classify the spatiotemporal BSPM data and further localize the abnormal ventricular activation. Li and He *et al.* [11] and Farina *et al.* [12] proposed to determine the optimal extent and location of a spherical MI by minimizing the differences between the real-world BSPM data and the BSPM simulated from a heart model with infarctions. SadAbadi *et al.* [13] developed a location relationship between the positions of BSPM sensors and regions of the heart, and further characterized the extent and location of MIs by investigating abnormal features in BSPM. Mneimneh *et al.* [14] proposed to use a reconstructed phase space and a Gaussian mixture model to create a multi-dimensional representation of the BSPMs to differentiate the electrical signals from healthy and infarct segments of the human heart, and further quantify the MIs on the heart surface.

Although BSPMs provides the high-resolution distribution of electric potentials on the body surface, cardiac electrical activity is often blurred while propagating from the heart to the body, which diminishes important spatiotemporal characteristics pertinent to the MIs. The characterization methods by investigating BSPMs are therefore limited in the ability to quantify the extent and location of MIs on the heart surface. In order to delineate pathological changes in the heart, medical scientists call for the estimation of heart-surface electrograms from the high-resolution BSPMs and the complex torso-heart geometry, i.e., the inverse ECG problem.

B. Inverse ECG Problem

The inverse ECG model is proposed to reconstruct heart-surface electrograms from BSPMs, and is further used to non-invasively image electrical activities of the heart. Two source models are commonly used in the inverse ECG problems. The first source model is called "action-based model", where

the dominant feature of cardiac electrical activity is assumed to be the arrival timing of the depolarization wavefront at each location in the heart. In this model, the entire heart is modeled with finite element method instead of the epicardial surface [15], [16]. For example, Wang *et al.* [17] modeled the inverse ECG problem by constraining the solution on the electrophysiological model, i.e., the reaction-diffusion model, that guides the propagation of potential and recovery current.

The second source model is called "potential-based" model, which assumes that cardiac sources are represented by time-varying electrical potentials on the heart surface. Electromagnetic theory is integrated with boundary element method to model the relationship between potential distributions on the body and heart surfaces [9], [18]. Cheng *et al.* [19] compared the two source models and found there are no significant differences between the reconstructed heart-surface potentials. Nonetheless, the "activation-based" model requires modeling the entire heart, which introduces more imaging and computational efforts than the "potential-based" model [15], [20].

The present investigation will focus on the "potential-based" model. The relationship between the potential distributions on the body and heart surfaces is represented by a transfer matrix $\boldsymbol{R}_{BH}$. In order to calculate $\boldsymbol{R}_{BH}$, the human body is first modeled as a source-free homogeneous volume conductor, whose boundary consists of the heart and body surfaces. Second, the boundary element method is implemented to discretize the heart and body surfaces [21]. Finally, the electric potentials on the two surfaces are related by:

$$\boldsymbol{\phi}_B = \boldsymbol{R}_{BH}\boldsymbol{\phi}_H \tag{1}$$

in which $\boldsymbol{\phi}_B$ and $\boldsymbol{\phi}_H$ denote the potential distributions on the body and heart surfaces, respectively, and $\boldsymbol{R}_{BH}$ incorporates both the torso-heart geometries and the electrical conducting properties of the human body [22].

However, the inverse ECG problem involves dynamic potentials distributed on the complex heart and body surfaces, and is generally ill-conditioned. The transfer matrix $\boldsymbol{R}_{BH}$ is with large condition number (i.e., $cond(\boldsymbol{R}_{BH}) = \|\boldsymbol{R}_{BH}^{-1}\|\|\boldsymbol{R}_{BH}\|$), indicating that a small noise $\Delta\boldsymbol{\phi}_B$ in $\boldsymbol{\phi}_B$ caused by measurement equipment will result in a big difference $\Delta\boldsymbol{\phi}_H$ in the estimation of $\boldsymbol{\phi}_H$ (i.e., $\frac{\Delta\boldsymbol{\phi}_H}{\boldsymbol{\phi}_H} \simeq cond(\boldsymbol{R}_{BH})\frac{\Delta\boldsymbol{\phi}_B}{\boldsymbol{\phi}_B}$). To address this problem, different methods have been proposed, such as Tikhonov L2-norm [23] and L1-norm regularization methods [24], [25]. These methods solve the inverse ECG problem individually at each time point, and do not account for temporal correlations among the time-varying electric potentials.

Brooks *et al.* [18] proposed to increase the spatial and temporal regularity of the inverse solution by simultaneously constraining the magnitude or second-order spatial derivative and the first-order temporal derivative of heart-surface potentials. In order to solve the proposed model, they reformulated the problem with an augmented model, which resulted in a matrix representation with the dimension of $(N * T) \times (N * T)$, where N is the number of nodes on the heart surface and T is the length of the time series. The computation involves complex matrix-operations and the complexity will increase when the dimension (N or T) is getting large.

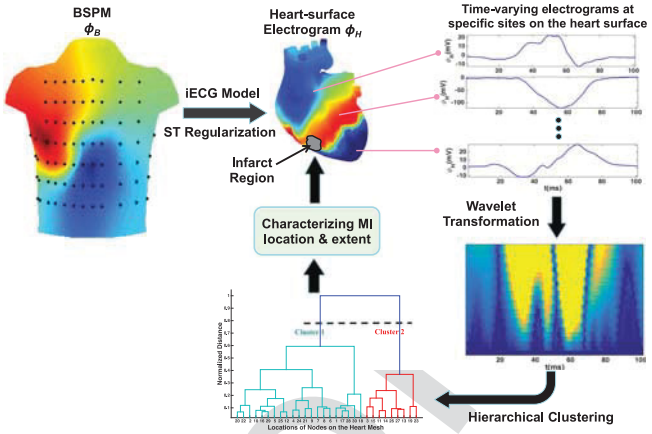

Fig. 1. The flowchart of research methodology.

Messnarz *et al.* [26] estimated cardiac electric potentials using a spatiotemporal approach, in which they accounted for the spatial correlation by a symmetric gradient matrix, and formulate the temporal constraint assuming that the potential signals are monotonically nonincreasing during depolarization phase. However, the torso-heart geometry is highly complex, and a symmetric matrix tends to be limited to approximate the surface gradient. Moreover, the nondecreasing assumption in the temporal constraint may not be generally applicable to real-world inverse ECG model.

Our previous work proposed a spatiotemporal regularization (STRE) model to solve the high-dimensional inverse ECG problem [9]. We define a surface Laplacian for irregular triangle meshes to improve the spatial regularity of the inverse solution, and account for the temporal correlation by constraining the sum-of-square of the differences in potential signals in a small time window. In addition, we proposed an iterative method of dipole multiplicative update to solve the STRE model, which is inspired by the dipole assumption in electrodynamic physics.

However, very little has been done to identify and characterize MIs on the heart surface using the spatiotemporal regularization method. In this investigation, we utilize the STRE framework to solve the inverse ECG problem from BSPMs and torso-heart geometry, and further quantify the extent and location of MIs on the heart surface using a wavelet-clustering method.

III. Research Methodology

As shown in Fig. 1, this paper presents the application of spatiotemporal inverse ECG (ST-iECG) modeling to characterize the location and extent of MIs. First, we reconstruct the time-varying heart-surface electrograms from BSPMs using the inverse ECG modeling and spatiotemporal regularization method. Second, heart-surface electrograms are decomposed into multiple frequency bands through the wavelet transformation. This time-frequency decomposition provides salient features to represent disease-altered patterns in heart-surface electrograms. Finally, we performed the hierarchical clustering of wavelet coefficients to delineate the grouping behavior of heart-surface electrograms, which further help characterize the extent and location of MIs.

A. Spatiotemporal Regularization

BSPMs provide high-resolution distribution of electric potentials over the entire torso to delineate the spatiotemporal dynamics in the heart. Little has been done to reconstruct the electric potentials on the heart surface from BSPMs using spatiotemporal regularization method and further quantify the MIs. In the present investigation, we solve the inverse ECG problem from BSPMs and the torso-heart geometries using the STRE model, and will characterize the extent and location of MIs by investigating the reconstructed heart-surface electrograms. The objective function of the STRE model [9] is as follows:

$$\min_{\boldsymbol{\phi}_H(t)} J = \sum_{t=1}^{T}\{\|\boldsymbol{\phi}_B(t) - \boldsymbol{R}_{BH}\boldsymbol{\phi}_H(t)\|^2 + \lambda_s^2\|\Delta_s\boldsymbol{\phi}_H(t)\|^2 + \lambda_t^2 \sum_{\tau=t-\frac{w}{2}}^{t+\frac{w}{2}} \|\boldsymbol{\phi}_H(t) - \boldsymbol{\phi}_H(\tau)\|^2\} \quad (2)$$

where λ_s and λ_t are the spatial and temporal regularization parameters, respectively, which are chosen by L-curve method [27] or cross validation. The matrix Δ_s represents the spatial Laplacian operator of irregular triangle meshes and is proposed to improve the spatial regularity of the estimated potentials on the heart surface. The sum-of-square of the differences in electrical potentials in a time window w, i.e., the third term in (2), is proposed to increase model robustness to measurement noises in the time domain.

The STRE model involves both the spatial and temporal correlations among the electric potential ϕ_H, and it is difficult to solve for ϕ_H analytically. In our previous work, we propose to estimate ϕ_H using the iterative method of dipole multiplicative update (DMU) inspired by the dipole assumption in electrodynamic physics. Briefly, the DMU method splits the electric potential $\boldsymbol{\phi}_H$ into its positive part $\boldsymbol{\phi}_H^+$ and negative part $\boldsymbol{\phi}_H^-$, where $\boldsymbol{\phi}_H^+$ and $\boldsymbol{\phi}_H^-$ are defined as $\boldsymbol{\phi}_H^+ = \max\{0, \boldsymbol{\phi}_H\}$ and $\boldsymbol{\phi}_H^- = \max\{0, -\boldsymbol{\phi}_H\}$. And then, we can write $\boldsymbol{\phi}_H$ as $\boldsymbol{\phi}_H = \boldsymbol{\phi}_H^+ - \boldsymbol{\phi}_H^-$, and obtain the updating rules for $\boldsymbol{\phi}_H^+$ and $\boldsymbol{\phi}_H^-$ in the algorithm shown in Table I (see details in [9]).

B. Wavelet Decomposition of Heart-Surface Electrograms

The time series data such as heart-surface electrograms $\boldsymbol{\phi}_H$ are generally characterized by high dimensionality, high correlation, uncertainties and measurement noises. Traditional time-domain investigation tends to overlook hidden information inherent in original signals (e.g., spatial information pertinent to MIs). Frequency-domain analysis such as Fourier transformation identifies spectral components present in the signal but does not provide temporal localization of these components. Methods of time-frequency analysis such as wavelet transformation provide interpretation of time series in both time and frequency simultaneously, which enables the delineation of local, transient or intermittent components inherent to the data.

In the present investigation, we propose to transform the electrograms on the heart surface with the Daubechies wavelet [28]. Note that most of the previous works show that the closer the wavelet functions match the signal pattern, the more compact the representation will be [29]. The heart electrogram $\boldsymbol{\phi}_H$ is denoted as $\{\phi_H(t)\}_{t=1}^T$ and is decomposed into the running averages $A_j(k)$ to approximate the original time sequence, and running differences $D_j(k)$ to characterize the details of the time series $\boldsymbol{\phi}_H$, where $j = 1, 2, \ldots$ denotes the decomposition level (i.e., scaling value) and $k = 1, 2, \ldots$ represents the position (i.e., translation value). $A_j(k)$ and $D_j(k)$ are defined recursively as

$$A_j(k) = \sum_{t=1}^{T} h_j A_{j-1}\left((2k+t) \mod 2^{j+2}\right) \quad (3)$$

$$D_j(k) = \sum_{t=1}^{T} (-1)^t h_j A_{j-1}\left((2k+2T-t) \mod 2^{j+2}\right) \quad (4)$$

$$A_1(k) = \sum_{t=1}^{T} \phi(t) V_n(t-k) \quad (5)$$

where h_j's are filter coefficients of the Daubechies scaling function, and the scaling function $V_n(t)$ and wavelet function $W_n(t)$ are defined recursively as

$$V_n(t) = \sqrt{2}\sum_{k=0}^{2n-1} h_k V_n(2t-k) \quad (6)$$

$$W_n(t) = \sqrt{2}\sum_{k=0}^{2n-1} (-1)^k h_{2n-1-k} V_n(2t-k) \quad (7)$$

Thus, at level j of decomposition, ϕ_H is expressed as

$$\phi_H(t) = \sum_k A_j(k) V_n\left(\frac{t}{2^j} - 2^j k\right) + \sum_{j'=1}^{j}\sum_k D_{j'}(k) W_n\left(\frac{t}{2^{j'}} - 2^{j'} k\right) \quad (8)$$

The wavelet decomposition provides an effective framework of multi-resolution analysis for investigating the heart-surface electrogram $\boldsymbol{\phi}_H$ at various levels of approximations A_j's and details D_j's. This multi-resolution framework will better elucidate both the local and transient characteristics of $\boldsymbol{\phi}_H$ that are often obscured by the traditional time-domain or frequency-domain analysis.

C. Hierarchical Clustering

Hierarchical clustering (HC) algorithm is further used to cluster each sequence of running average A_j's and running difference D_j's of heart-surface electrogram $\phi_H(t)$ at different level j. The HC algorithm creates a hierarchical decomposition of the input data represented by a dendrogram. The dendrogram is constructed according to the $N \times N$ distance (similarity) matrix given by the N observations (i.e., N ECG time series) in the dataset. (Note in the present investigation, N is the number of nodes on the heart surface.) At the first step of HC, each observation is assigned to its own cluster, which results in N singleton clusters. Then, the closest (i.e., most similar) pair

TABLE I
THE PROPOSED DIPOLE MULTIPLICATIVE UPDATE ALGORITHM

1: Set constants λ_s, λ_t and w .
2: Initialize $\{\phi_H^+\}$ and $\{\phi_H^-\}$ as positive random matrices: whose columns (rows) denote different time points (different nodes on the heart surface)
3: **Repeat**
4: **for** $t = 1, \ldots, T$ **do**

$$(\phi_{H,t}^+)_i \leftarrow \frac{(\boldsymbol{A}\phi_{H,t}^-)_i + B_i + \sqrt{((\boldsymbol{A}\phi_{H,t}^-)_i + B_i)^2 + 4(\boldsymbol{A}^+\phi_{H,t}^+)_i(\boldsymbol{A}^-\phi_{H,t}^+)_i}}{(2\boldsymbol{A}^+\phi_{H,t}^+)_i}(\phi_{H,t}^+)_i$$

$$(\phi_{H,t}^-)_i \leftarrow \frac{(\boldsymbol{A}\phi_{H,t}^+)_i - B_i + \sqrt{((\boldsymbol{A}\phi_{H,t}^+)_i - B_i)^2 + 4(\boldsymbol{A}^+\phi_{H,t}^-)_i(\boldsymbol{A}^-\phi_{H,t}^-)_i}}{(2\boldsymbol{A}^+\phi_{H,t}^-)_i}(\phi_{H,t}^-)_i$$

where

$$\boldsymbol{A} = \boldsymbol{R}_{BH}^T\boldsymbol{R}_{BH} + \lambda_s^2\Delta_s^T\Delta_s + 2\lambda_t^2 w\boldsymbol{I}$$

$$\boldsymbol{B} = \phi_B^T(t)\boldsymbol{R}_{BH} + 2\lambda_t^2\sum_{\tau=t-w/2}^{t-1}\phi_H^T(\tau) + 2\lambda_t^2\sum_{\tau=t+1}^{t+w/2}\phi_H^T(\tau)$$

5: **end for**
6: **until convergence**

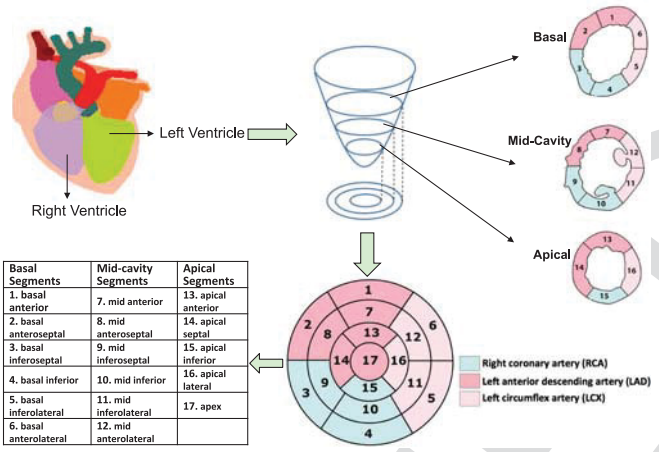

Basal Segments	Mid-cavity Segments	Apical Segments
1. basal anterior	7. mid anterior	13. apical anterior
2. basal anteroseptal	8. mid anteroseptal	14. apical septal
3. basal inferoseptal	9. mid inferoseptal	15. apical inferior
4. basal inferior	10. mid inferior	16. apical lateral
5. basal inferolateral	11. mid inferolateral	17. apex
6. basal anterolateral	12. mid anterolateral	

Fig. 2. 17-segment model of the left ventricle.

of clusters is merged into one single cluster. The recursive merging strategy continues to move up the hierarchy until all the observations are clustered into one single cluster of size N.

The optimal number of clusters is chosen by the Silhouette index. Let $\mathcal{C} = \{C_1, \ldots, C_K\}$ denote the K clusters of the data set. The j^{th} cluster is defined as $C_j = \{\phi_1^j(t), \ldots, \phi_{n_j}^j(t)\}$, and $n_j = |C_j|$ is the cardinality of the j^{th} cluster. Let $d(\phi_k(t), \phi_l(t))$ denote the distance between $\phi_k(t)$ and $\phi_l(t)$. Then the Silhouette index with K clusters is defined as:

$$S_K = \frac{1}{K}\sum_{j=1}^{K}\frac{1}{n_j}\sum_{j=1}^{n_j}\frac{b_i^j - a_i^j}{\max\{a_i^j, b_i^j\}} \tag{9}$$

where a_i^j is the average distance between the i-th observation in cluster C_j and the other observations in the same cluster, b_i^j denotes the minimum average distance between the i-th observation in C_j and all the observations in C_k, $k = 1, \ldots, K$, $k \neq j$.

$$a_i^j = \frac{1}{n_j - 1}\sum_{k=1, k\neq i}^{n_j} d(\phi_i^j(t), \phi_k^j(t)) \tag{10}$$

$$b_i^j = \min_{m=1,\ldots,K, m\neq j}\left\{\frac{1}{n_m}\sum_{k=1}^{n_m} d(\phi_i^j(t), \phi_k^m(t))\right\} \tag{11}$$

The value of S_K is between -1 and 1, and a bigger S_K indicates better clustering result. Therefore, the optimal number of cluster K^* is chosen as

$$K^* = \arg\max_K S_K \tag{12}$$

Furthermore, A_j's and D_j's are clustered into K^* clusters using the HC algorithm. The clustering results are further used to characterize the extent and location of MIs on the heart surface in the experiment.

D. Performance Metrics

Gadolinium-enhanced transaxial MRI (GE-MRI) images provide the golden standards to evaluate the performance of the ST-iECG model. The extent, centroid and location of infarction area on the heart surface are presented by the 17-segment model [30] as shown in Fig. 2. In the 17-segment model, the left ventricle (LV) is first segmented into three coarse parts: basal, apical and mid-cavity along its long axis from the apex of LV to the base. Furthermore, the basal area and the mid-cavity are divided into six finer segments, respectively, and the apical area is divided into four finer segments. The name of each segment is displayed in Fig. 2.

Three performance metrics are defined to evaluate the performance of the proposed ST-iECG model:

1) **EPD**-percentage discrepancy between the extent of infarction as estimated and as given by GE-MRI images;
2) **SO**-overlap percentage between infarct segments as estimated and as given by GE-MRI images;

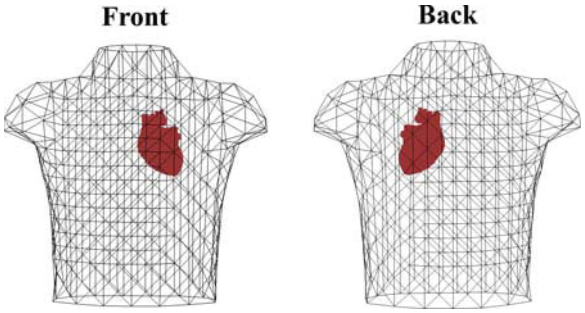

Fig. 3. Torso-heart geometry.

3) **CED**-distance from the centroid of the infarct area as given by GE-MRI images to that as estimated.

The three metrics of the proposed ST-iECG model are further benchmarked with the results provided by the existing iECG model [23] in the next section.

IV. Experimental Design and Results

A. Dataset

The dataset in this investigation including the customized torso-heart geometry (as shown in Fig. 3) and body surface potential mapping (BSPM) is sourced from the PhysioNet website [23], [31]. The BSPMs are collected from four patients who carried one-year MIs, which contain time series of electric potentials from 0 to 1000 ms at 352 locations on the body surface. These four cases are split into two training cases and two test cases. The true MI segments for each patient are outlined by the GE-MRI images, which provides the reference for evaluating the performance of the ST-iECG model.

B. The Impact of Mesh Resolution on Inverse ECG Modeling

In potential-based inverse ECG problem, the transfer matrix $\boldsymbol{R}_{BH}$ is computed by integrating electromagnetic theory and boundary element method (BEM). In BEM, the torso-heart geometries are discretized into triangle meshes to numerically solve the Laplacian equation that establishes the relationship between ϕ_H and ϕ_B. The solution integrals are approximated by the summation of a series of numerical integrations over triangle elements. The approximation accuracy is closely dependent on the mesh resolution, which impacts the estimation of the inverse ECG problem. Few, if any previous works studied the effects of mesh resolution on the inverse ECG solution. At the present investigation, we study the effects of mesh resolution on the solution to inverse models in order to find the optimal mesh resolution [21].

We vary the number of elements N_T on the triangle mesh of the heart surface by setting it to be 136, 272, 408, 546, 654, 872 and 1092. Fig. 4 is an illustration of the triangle mesh and the 3D heart model. Under different mesh resolution, we solve the inverse problem and investigate the variation of mean squared error (MSE) with respect to N_T as shown in Fig. 5. Note that in order to calculate MSE, the estimated heart-surface potential $\boldsymbol{\phi}_H(t)$ is used to predict the body-surface potential from the forward ECG model, i.e., $\hat{\boldsymbol{\phi}}_B(t) = \boldsymbol{R}_{BH}\boldsymbol{\phi}_H(t)$. Then the MSE is computed as

$$MSE = \frac{\sum_{t=1}^{T} \|\hat{\boldsymbol{\phi}}_B(t) - \boldsymbol{\phi}_B(t)\|}{T \times N_B} \quad (13)$$

where $\boldsymbol{\phi}_B(t)$ is real data of body-surface potentials, T is the length of time series, and N_B is the number of nodes on the body surface.

According to Fig. 5, the MSE decreases as the number of triangles increases. Moreover, when N_T exceeds 400, the value

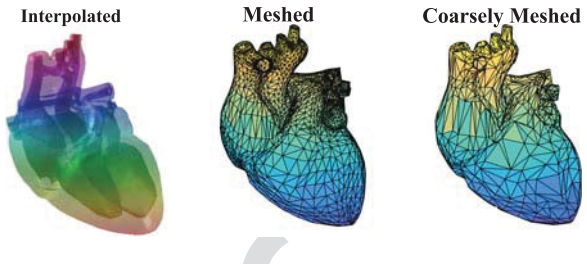

Fig. 4. Illustration of the interpolated 3D heart model and triangle meshes of the heart surface.

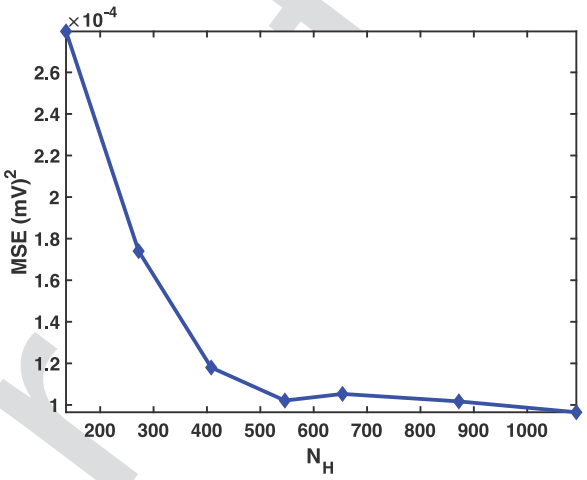

Fig. 5. The variation of mean squared errors with respect to the number of triangle elements N_T on the heart mesh.

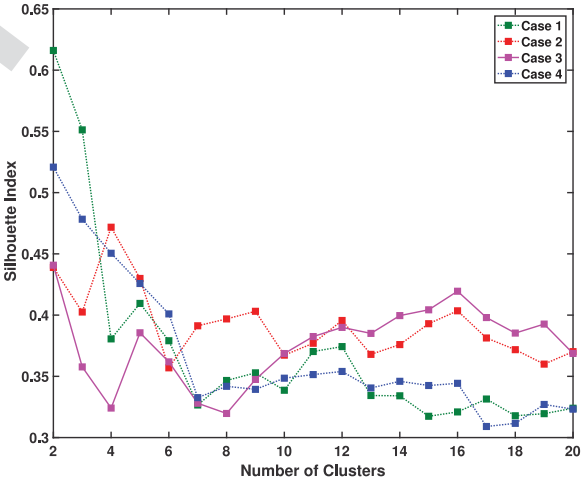

Fig. 6. The variation of Silhouette index with respect to different number of clusters for the 4 cases.

TABLE II
RESULTS OF MI CHARACTERIZATION WITH WAVELET CLUSTERING IN TRAINING CASE 1 AND CASE 2

MI Characterization		GE-MRI	Signal	A1	A2	A3	A4	A5	A6	D1	D2	D3	D4	D5	D6
Case 1	Extent	31%	24%	34%	34%	**32%**	22%	24%	25%	61%	38%	23%	40%	26%	26%
	MI segments	1, 2, 3, 8, 9, 13, 14, 15	1, 2, 3, 8, 9, 13, 15, 16	2,3,5,7,8,9, 11,13,14	1, 2, 3, 8, 9, 13, 15, 16	**1,2,3,8,9,13 ,15,16**	1, 2, 3, 8, 9, 13, 15, 16	1, 2, 3, 8, 9, 13, 15, 16	1, 2, 3, 8, 9, 13, 15, 16	1,2,3,4,5,7, 8,9,12,13,1 4,15,17	1,2,3,5,7,8, 11,12,13,14 ,15,17	2,3,6,8,9,10 ,14	1,2,3,5, 8,9,11,12,1 3,14,17	1,2,3,4,7,8, 9,14,15,16	1,2,3,4,7,8, 9,14,15,16
	Centroid	8	8	8 or 9	8	**8**	8	8	8	14	13	9	14	8 or 9	8 or 9
	EPD	-	7%	3%	3%	**1%**	9%	7%	6%	30%	7%	8%	9%	5%	5%
	SO	-	67%	50%	67%	**67%**	67%	67%	67%	56%	50%	45%	54%	58%	58%
	CED	-	0	0	0	**0**	0	0	0	1	2	0	0	0	0
Case 2	Extent	30%	17%	19%	28%	**20%**	18%	28%	36%	43%	21%	36%	43%	26%	31%
	MI segments	3, 4, 9, 10	3,5,9,10	3,5,9,10	1,3,5,9,10,1 3	**3,5,9,10**	3,5,9,10	1,3,4,7,9,15 ,17	1,3,5,7,9,10 ,13,14,15	1,3,4,7,9,10 ,12,13,15,1 6	3,4,7,9,15	1,3,5,9,10,1 1,14,17	1,2,5,7,9,10 ,11,13,17	1,3,4,7,9,10 ,15	1,3,4,7,9,10 ,15
	Centroid	3 or 4 or 9 or 10	10	10	9	**10**	10	9	14	15	9	10	13	15	15
	EPD	-	13%	11%	2%	**10%**	12%	2%	6%	13%	9%	6%	13%	4%	1%
	SO	-	60%	60%	42%	**60%**	60%	37.50%	30%	40%	50%	33%	18%	57%	57%
	CED	0	0	0	0	**0**	0	0	1	1	0	0	3	1	1

of MSE remains relatively stable and little improvement can be achieved if we further increase the number of triangle elements. The value of N_T should be greater than 400 to guarantee the accuracy of the inverse model, but should not be very large to make the inverse model computationally expensive. In this investigation, we therefore set the number of mesh elements triangulating the heart surface to be 546, which is the elbow point between $N_T = 500$ and $N_T = 600$.

C. MI Characterization With Wavelet Clustering

The body surface consists of 677 triangle elements and 352 nodes, and the heart surface is formed with 546 triangle elements and 275 nodes, which results in a 352×275 transfer matrix $\boldsymbol{R}_{BH}$. The ST-iECG method with λ_s=0.06, $\lambda_t = 0.005$ chosen by L-curve method and $w = 2$ is implemented to solve the potential distribution ϕ_H on the heart surface. The QRS interval (represents ventricular depolarization) of estimated potential signals on the heart surface are grouped into different clusters by the HC algorithm with the cluster number varying from 2 to 20. Note that we conducted experiments to study different segments of heart-surface electrograms, including the entire ECG cycle, P wave, QRS wave, and T wave. Experimental results show that clustering of QRS wave yields the best characterization results. This agrees with the fact that QRS wave corresponds to the ventricular depolarization. Therefore, in this investigation we characterize the MIs using the QRS waves of the heart-surface electrograms.

Fig. 6 shows the variation of Silhouette index with respect to the cluster number of the four cases. Notably, cases 1, 3 and 4 yield the highest Silhouette index when the number of clusters is two. This shows that two different clusters exist in the heart-surface electrograms. One cluster denotes signals from healthy segments and the other represents signals from infarct segments on the heart surface. In case 2, the Silhouette index is higher with four clusters than that with two clusters. This may be due to the existence of inhomogeneous tissues and cellular structures in the infarction regions of case 2. Such inhomogeneity leads to more variations in heart-surface electrograms, which can be further partitioned into sub-clusters. In other words, the big cluster is further split into three sub-clusters. In the present investigation, the number of cluster is selected as two so as to achieve the overall highest Silhouette index for four cases.

The calculated ϕ_H in training case 1 and case 2 is further decomposed into running averages A_j's and running difference D_j's with $j = 1, 2, 3, 4, 5, 6$ by Daubechies wavelet. The estimated signal ϕ_H, each A_j and D_j are grouped into two clusters by the HC algorithm. Table II shows the characterization results estimated by the wavelet-clustering method and the reference results given by the GE-MRI images. Note that characterization of MIs by the approximation levels A_j's generally yield better performance metrics, i.e., lower EPD, higher SO, and lower CED. This suggests that the characteristics in transient parts (high-frequency details, D_j's) in the heart electrograms may not relate to useful information pertinent to MIs. It is worth noting that in training case 1, A3 (i.e., the approximation at level $j = 3$) yields the smallest EPD of 1%, highest SO of 67%, and CED of zero. In training case 2, A3 yields a zero CED and the highest SO of 60%. Therefore, A_3 is chosen as the optimal representation of $\boldsymbol{\phi}_H$, and is grouped into healthy and infarct clusters to further characterize the MIs on the heart surface in later experiments.

D. Characterization Results in Training Case 1 and Case 2

Fig. 7(a) shows the average potential signals $\pm$ standard deviation of two clusters denoting onset of infarction and normal heart activity of training case 1 by the proposed ST-iECG model. Note that although significant variations exist in the clusters of onset of infarction and normal heart activity due to the heart geometry and disease complexity, the cluster colored in blue contains more positive signals, while the one in red consists of negative signals, particularly, a negative Q wave. Fig. 7(b) shows

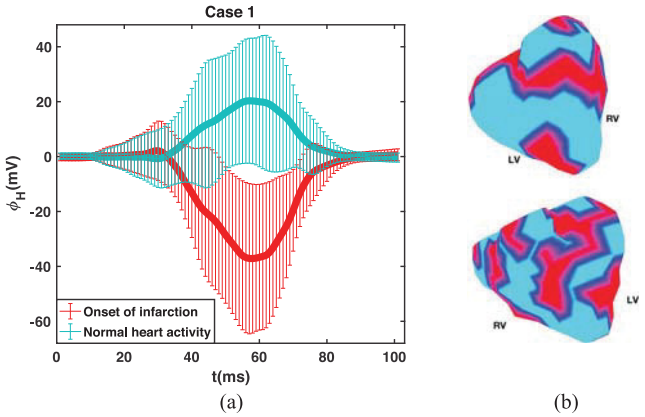

Fig. 7. (a) Average potential signals ± one standard deviation of the clusters of normal heart activity and onset of infarction in training case 1; (b) Color-coded distribution of the two clusters on the heart surface with inferior view (top) and anterosuperior view (bottom).

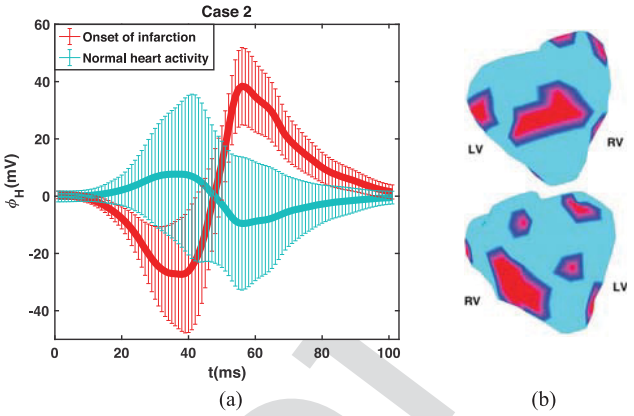

Fig. 9. (a) Average potential signals ± one standard deviation of the clusters of normal heart activity and onset of infarction in training case 2; (b) Color-coded distribution of the two clusters on the heart surface with inferior view (top) and anterosuperior view (bottom).

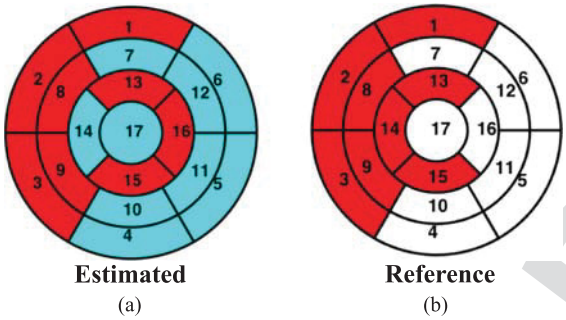

Fig. 8. (a) Estimated MIs (i.e., segments colored in red) by the proposed ST-iECG model of training case 1; (b) Reference MIs (i.e., segments colored in red) provided by the GE-MRI image of training case 1.

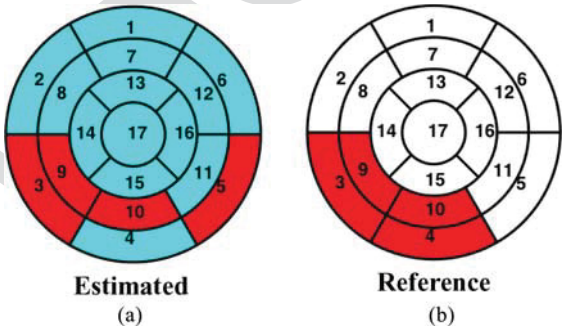

Fig. 10. (a) Estimated MIs (i.e., segments colored in red) by the proposed ST-iECG model of training case 2; (b) Reference MIs (i.e., segments colored in red) provided by the GE-MRI image of training case 1.

the color-coded 3D heart surface with red and blue colors representing the infarct and normal clusters respectively. The 3D heart surface is then projected into the 17-segment model, as shown in Fig. 8(a). The true infarct segments (colored in red) given by the GE-MRI image is shown in Fig. 8(b). By comparing the segments of each cluster estimated by the ST-iECG model with the true infarct segments, the red cluster, i.e., the one contains negative Q wave, is identified as the cluster of onset of infarction, while the blue one, i.e., the one contains more positive signals, is specified as the cluster of normal heart activity.

As shown in Fig. 8(a), the estimated infarct segments (i.e., the segments colored in red) are 1, 2, 3, 8, 9, 13, 15 and 16 in case 1. The true infarct segments given by GE-MRI image are 1, 2, 3, 8, 9, 13, 14 and 15 as shown in Fig. 8(b). The extent of infarction is obtained by dividing the number of the infarct nodes on the heart surface by the total number of nodes, which is 32% in case 1, and is close to the GE-MRI result of 31%. In addition, it can be noted from Fig. 8(a) that the centroid of the estimated infarct segments is segment 8, which matches the centroid given by the GE-MRI image.

Fig. 9(a) illustrates average potential signals ± one standard deviation of the clusters of normal heart activity and onset of infarction in training case 2 by the proposed ST-iECG model. Notably, the magnitude of negative potentials in the blue cluster is much smaller compared with that in the red cluster. Fig. 9(b) shows the color-coded heart surface with red and blue colors representing the two different clusters. The corresponding 17-segment model is shown in Fig. 10(a), and Fig. 10(b) shows the true infarct clusters (colored in red) given by the GE-MRI image. Comparing the two clusters estimated by the proposed ST-iECG model with the true infarct segments of case 2, the red cluster is identified as the infarct cluster, while the blue one denotes the normal cluster, which is consistent with the training result in case 1.

As shown in Fig. 10(a), the estimated infarct segments (i.e., segments colored in red) are 3, 5, 9 and 10 in case 2. The true infarct segments are 3, 4, 9 and 10 given by the GE-MRI image as shown in Fig. 10(b). The estimated extent of infarction in case 2 is 20% which is not too far away from 30% given by the GE-MRI analysis, and the estimated centroid is segment 10 matching the centroid given by GE-MRI image.

E. Characterization Results in Test Case 3 and Case 4

Fig. 11(a) shows the average potential signals ± one standard deviation of the two clusters representing onset of infarction and normal heart activity estimated by the proposed ST-iECG model in test case 3. According to the experimental results in training case 1 and case 2 in subsection D, the red cluster containing

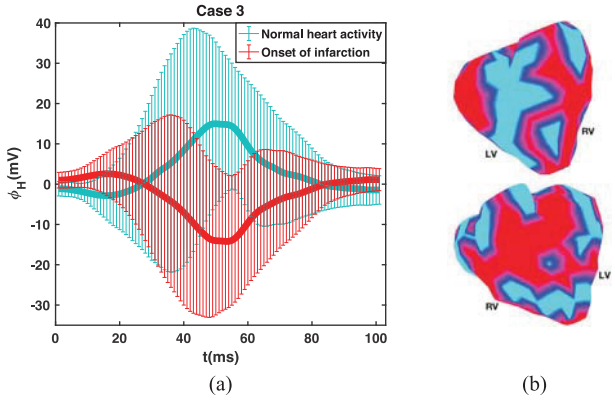

Fig. 11. (a) Average potential signals ± one standard deviation of the clusters of normal heart activity and onset of infarction in test case 3; (b) Color-coded distribution of the two clusters on the heart surface with inferior view (top) and anterosuperior view (bottom).

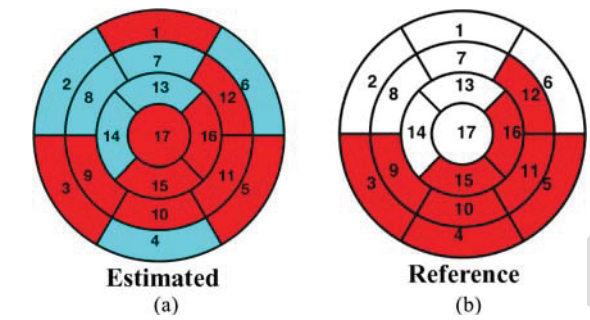

Fig. 12. (a) Estimated MIs (i.e., segments colored in red) by the proposed ST-iECG model of test case 3; (b) Reference MIs (i.e., segments colored in red) provided by the GE-MRI image of test case 3.

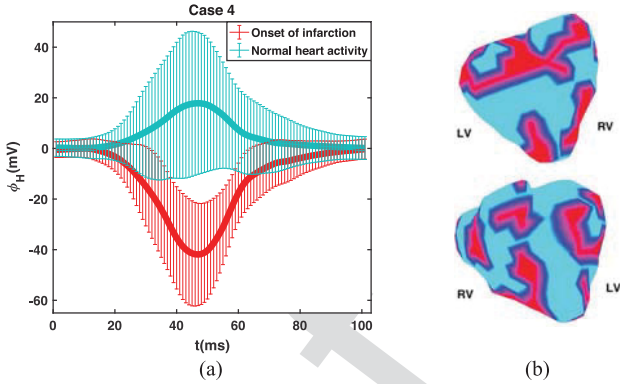

Fig. 13. (a) Average potential signals ± one standard deviation of the clusters of normal heart activity and onset of infarction in test case 4; (b) Color-coded distribution of the two clusters on the heart surface with inferior view (top) and anterosuperior view (bottom).

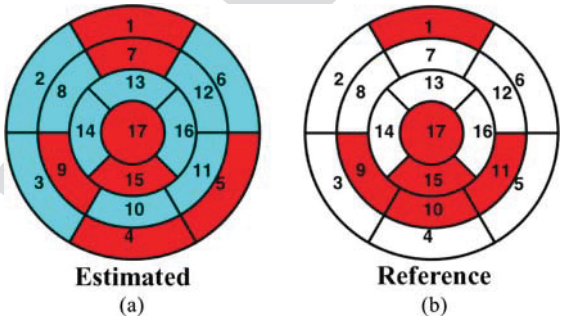

Fig. 14. (a) Estimated MIs (i.e., segments colored in red) by the proposed ST-iECG model of test case 4; (b) Reference MIs (i.e., segments colored in red) provided by the GE-MRI image of test case 4.

more negative signals is specified as infarct cluster, and the blue one with more positive signals is the cluster of normal heart activity. Fig. 11(b) illustrates the heart surface with the infarct areas colored in red and healthy area colored in blue. Projecting the heart surface into the 17-segment model, Fig. 12 shows the comparison of the infarct segments (colored in red) as estimated by the ST-iECG model and as given by the GE-MRI image. Note that the estimated infarct segments are 1, 3, 5, 9, 10, 11, 12, 15, 16 and 17. The extent of the estimated infarct area in case 3 is 51%, and the estimated centroid is segment 11 or 15.

Fig. 13(a) presents the clustering results in test case 4. The red cluster containing negative signals is specified as infarct cluster, and the blue one with positive signals is the normal cluster according to the training results in subsection D. Fig. 13(b) illustrates the infarct areas colored in red and the normal cluster colored in blue on the heart surface of case 4. Fig. 14 shows the comparison of the estimated infarct segments and reference result given by the GE-MRI image, after projecting the heart surface into the 17-segment model. Note that the estimated infarct segments are 1, 4, 5, 7, 9, 15 and 17. The extent and centroid of the estimated MI are 29% and segment 15, respectively.

Table III summarizes the reference results of MIs for all the four cases given by GE-MRI images, the estimated results given by the proposed ST-iECG model, and that estimated by the existing iECG model [23]. Table IV highlights the comparison of performance metrics (i.e., EPD, SO, and CED) in test case 3 and case 4 by the ST-iECG model with the iECG model [23]. The ST-iECG model yields a smaller EPD of 1% for case 3 and 15% for case 4 compared with the iECG model (i.e., 17% and 26% for case 3 and case 4, respectively), which suggests that the extent of estimated MIs is closer to the true results given by GE-MRI images. The SO estimated by the ST-iECG model is 0.727 in case 3 and 0.444 in case 4, and that estimated by the iECG model is 0.556 and 0.3 for case 3 and case 4, respectively, which indicates that our estimated infarction overlaps more with the true infarct area. Furthermore, our estimated CED's are zero in both case 3 and case 4, suggesting that the centers of the estimated infarction by the ST-iECG model match the true centers given by the golden standards in both test cases, while the estimated center by iECG is 1 and 2 segments away from the true centers in case 3 and case 4, respectively.

According to Tables III and IV, all the three performance metrics (i.e., EPD, SO and CED) given by the ST-iECG model score better compared with the existing iECG model [23]. It is worth noting that both the proposed ST-iECG and the iECG overestimate the segments and extent of MI in case 4. The segments of infarction in case 4 given by the GE-MRI images are 1, 9, 10, 11, 15, 17 as shown in Table III, and there are 6 segments of MI in total. However, the extent of MI covers only 14% of the heart surface. This suggests that the infarction area in case 4 is highly spread, which poses a great challenge to accurately characterize the MI.

TABLE III
RESULTS FROM THE PROPOSED ST-IECG MODEL, EXISTING IECG MODEL [23], AND GE-MRI IMAGES

Characteristic	Method	Case 1	Case 2	Case 3	Case 4
Extent	GE-MRI	31%	30%	52%	14%
	iECG	25%	35%	35%	40%
	ST-iECG	32%	20%	51%	29%
Infarct Segments	GE-MRI	1, 2, 3, 8, 9, 13, 14, 15	3,4,9,10	3, 4, 5, 9, 10, 11, 12, 15, 16	1,9,10,11,15,17
	iECG	2, 3, 8, 9, 14	3, 4, 5, 9, 10, 11	3, 4, 5, 10, 11	3, 4, 5, 6, 9, 10, 11
	ST-iECG	1, 2, 3, 8, 9, 13, 15, 16	3, 5, 9, 10	1, 3, 5, 9, 10, 11, 12, 15, 16, 17	1, 4, 5, 7, 9, 15, 17
Centroid	GE-MRI	8	3 or 9 or 4 or 10	10 or 11	15
	iECG	9	10	4	4
	ST-iECG	8	10	11 or 15	15

TABLE IV
COMPARISON OF PERFORMANCE METRICS OF THE PROPOSED ST-IECG MODEL AND THE EXISTING IECG MODEL [23]

Metric	Method	Case 3	Case 4
EPD	iECG	17%	26%
	ST-iECG	1%	15%
SO	iECG	0.556	0.3
	ST-iECG	0.727	0.444
CED	iECG	1	2
	ST-iECG	0	0

Notably, the estimated centroids by the proposed ST-iECG model in all the training and test cases match that given by GE-MRI images, while there are discrepancies in the extent and segments of infarction between the estimated and true results. One of the possible sources of the discrepancies might be the orientation mismatch between the body surface and the heart surface in the 3D torso-heart model. Another possible reason is that we use a customized torso-heart geometry in this investigation, but the torso-heart geometries may vary from person to person, which will introduce uncertainties and errors in the estimation. In addition, the reference results given by GE-MRI images are characterized in terms of the 17-segment model of the left ventricle, while the modeled heart surface consists of both the right and left ventricles. The electrical activity in the inter-ventricular segments is thus greatly blurred by the activities on the right ventricle. Nevertheless, our inverse model is able to provide valuable information on the centroid, location, and extent of MIs on the heart surface, which is important to support medical scientists to make intervention decisions for patients with heart disease.

V. CONCLUSIONS

Myocardial infarction (MI) is among the leading causes of death in the United States. It is imperative to identify and characterize MIs for the timely delivery of medical intervention and the improvement of the quality of life. Cardiac electrical activity propagates in space and evolves over time. Most existing work identifies heart abnormalities by analyzing time-domain ECG signals (e.g., 12-lead ECG) on the body surface for detecting ECG wave deflections (i.e., P, QRS, and T waves), but tend to overlook spatiotemporal dynamics in the heart. They are limited in the ability to identify and characterize the extent and location of MIs.

BSPMs provide high-resolution of spatiotemporal distribution of electrical potentials on the entire torso, and therefore provide richer information than 12-lead ECG. Little has been done to reconstruct the heart-surface electrograms from BSPMs using spatiotemporal regularization method and further characterize MIs. In this paper, we propose the ST-iECG method to characterize the location and extent of MIs on the heart surface. We solve the inverse ECG problem and reconstruct heart-surface electrograms from BSPMs using the STRE model. In addition, we propose a wavelet-clustering method to investigate the pathological behaviors of heart-surface electrograms to characterize the MIs.

The ST-iECG model is evaluated and validated with real data of MIs from 4 human subjects. First, we perform wavelet-clustering of electrograms on the heart surface for two training cases. Experimental results show that A3 (i.e., the approximation at level $j = 3$ of the Daubechies wavelet decomposition) of the QRS waves on the heart surface yields the best characterization of MIs based on golden standards by GE-MRI images. Second, we validate the characterization results with the other two test cases, and found that negative QRS waves in the heart-surface electrograms indicate potential regions of MI. The performance of the proposed ST-iECG model is described by three metrics, i.e., EPD, SO and CED, all of which score better compared with existing iECG model, and demonstrate strong potential as a decision-support tool to noninvasively investigate cardiac pathological activities.

One limitation of the present study lies in the sample size and the range of patients' characteristics, although there are a large number of heart-surface electrograms in the healthy and infarction regions in each of four cases. The availability of BSPM data and GE-MRI images helps mitigate this limitation to some extent in the evaluation and validation experiments. In the future work, it is necessary to include more patients with healthy status and patients with mild and severe MIs in the investigation before fully establishing the utility of proposed methods for clinical applications.

ACKNOWLEDGMENT

The authors would also like to thank editors and anonymous reviewers for their constructive comments and suggestions to improve the quality of this paper.

REFERENCES

[1] E. J. Benjamin *et al.*, "Heart disease and stroke statistics 2017 update: A report from the american heart association," *Circulation*, vol. 135, no. 10, pp. e146–e603, 2017.

[2] H. P. Adams *et al.*, "Guidelines for the early management of patients with ischemic stroke," *Stroke*, vol. 34, no. 4, pp. 1056–1083, 2003.

[3] H. Engblom *et al.*, "The relationship between electrical axis by 12-lead electrocardiogram and anatomical axis of the heart by cardiac magnetic resonance in healthy subjects," *Amer. Heart J.*, vol. 150, no. 3, pp. 507–512, 2005.

[4] H. Yang, C. Kan, G. Liu, and Y. Chen, "Spatiotemporal differentiation of myocardial infarctions," *IEEE Trans. Autom. Sci. Eng.*, vol. 10, no. 4, pp. 938–947, Oct. 2013.

[5] H. Yang and F. Leonelli, "Self-organizing visualization and pattern matching of vectorcardiographic QRS waveforms," *Comput. Biol. Med.*, vol. 79, pp. 1–9, 2016.

[6] H. Yang, S. T. Bukkapatnam, and R. Komanduri, "Spatiotemporal representation of cardiac vectorcardiogram (VCG) signals," *Biomed. Eng. Online*, vol. 11, no. 2, pp. 16–30, 2012.

[7] Y. Rudy and J. E. Burnes, "Noninvasive electrocardiographic imaging," *Ann. Noninvasive Electrocardiology*, vol. 4, no. 3, pp. 340–359, 1999.

[8] Y. Rudy, "Electrocardiographic imaging: A noninvasive imaging modality for characterization of intramural myocardial activation," *J. Electrocardiology*, vol. 32, no. Suppl. 1, pp. 1–6, 1999.

[9] B. Yao and H. Yang, "Physics-driven spatiotemporal regularization for high-dimensional predictive modeling: A novel approach to solve the inverse ECG problem," *Sci. Rep.*, vol. 6, 2016, Art. no. 39012.

[10] K. Simelius *et al.*, "Spatiotemporal characterization of paced cardiac activation with body surface potential mapping and self-organizing maps," *Physiological Meas.*, vol. 24, no. 3, pp. 805–816, 2003.

[11] G. Li and B. He, "Non-invasive estimation of myocardial infarction by means of a heart-model-based imaging approach: A simulation study," *Med. Biol. Eng. Comput.*, vol. 42, no. 1, pp. 128–136, 2004.

[12] D. Farina and O. Dossel, "Model-based approach to the localization of infarction," in *Proc. 2007 Comput. Cardiology*, IEEE, 2007, pp. 173–176.

[13] H. SadAbadi *et al.*, "Variation of ECG features on torso plane: An innovative approach to myocardial infarction detection," in *Proc. 2007 Comput. Cardiology*, IEEE, 2007, pp. 629–632.

[14] M. Mneimneh and R. Povinelli, "RPS/GMM approach toward the localization of myocardial infarction," in *Proc. 2007 Comput. Cardiology*, IEEE, 2007, pp. 185–188.

[15] A. Pullan, L. Cheng, M. Nash, C. Bradley, and D. Paterson, "Noninvasive electrical imaging of the heart: Theory and model development," *Ann. Biomed. Eng.*, vol. 29, no. 10, pp. 817–836, 2001.

[16] P. M. Van Dam, T. F. Oostendorp, A. C. Linnenbank, and A. Van Oosterom, "Non-invasive imaging of cardiac activation and recovery," *Ann. Biomed. Eng.*, vol. 37, no. 9, pp. 1739–1756, 2009.

[17] L. Wang, H. Zhang, K. C. Wong, H. Liu, and P. Shi, "Physiological-model-constrained noninvasive reconstruction of volumetric myocardial transmembrane potentials," *IEEE Trans. Biomed. Eng.*, vol. 57, no. 2, pp. 296–315, Feb. 2010.

[18] D. H. Brooks, G. F. Ahmad, R. S. MacLeod, and G. M. Maratos, "Inverse electrocardiography by simultaneous imposition of multiple constraints," *IEEE Trans. Biomed. Eng.*, vol. 46, no. 1, pp. 3–18, Jan. 1999.

[19] L. K. Cheng, J. M. Bodley, and A. J. Pullan, "Comparison of potential-and activation-based formulations for the inverse problem of electrocardiology," *IEEE Trans. Biomed. Eng.*, vol. 50, no. 1, pp. 11–22, Jan. 2003.

[20] B. Erem, J. Coll-Font, R. M. Orellana, P. St'ovicek, and D. H. Brooks, "Using transmural regularization and dynamic modeling for noninvasive cardiac potential imaging of endocardial pacing with imprecise thoracic geometry," *IEEE Trans. Med. Imag.*, vol. 33, no. 3, pp. 726–738, Mar. 2014.

[21] B. Yao, S. Pei, and H. Yang, "Mesh resolution impacts the accuracy of inverse and forward ECG problems," in *Proc. 2016 IEEE 38th Annu. Int. Conf. Eng. Med. Biol. Soc.*, IEEE, 2016, pp. 4047–4050.

[22] R. C. Barr, M. Ramsey, and M. S. Spach, "Relating epicardial to body surface potential distributions by means of transfer coefficients based on geometry measurements," *IEEE Trans. Biomed. Eng.*, vol. BME-24, no. 1, pp. 1–11, Jan. 1977.

[23] F. Dawoud, G. S. Wagner, G. Moody, and B. M. Horáček, "Using inverse electrocardiography to image myocardial infarction-reflecting on the 2007 PhysioNet/Computers in cardiology challenge," *J. Electrocardiology*, vol. 41, no. 6, pp. 630–635, 2008.

[24] S. Ghosh and Y. Rudy, "Application of l1-norm regularization to epicardial potential solution of the inverse electrocardiography problem," *Ann. Biomed. Eng.*, vol. 37, no. 5, pp. 902–912, 2009.

[25] G. Shou, L. Xia, F. Liu, M. Jiang, and S. Crozier, "On epicardial potential reconstruction using regularization schemes with the l1-norm data term," *Phys. Med. Biol.*, vol. 56, no. 1, pp. 57–72, 2010.

[26] B. Messnarz, B. Tilg, R. Modre, G. Fischer, and F. Hanser, "A new spatiotemporal regularization approach for reconstruction of cardiac transmembrane potential patterns," *IEEE Trans. Biomed. Eng.*, vol. 51, no. 2, pp. 273–281, Feb. 2004.

[27] P. C. Hansen and D. P. O'Leary, "The use of the l-curve in the regularization of discrete ill-posed problems," *SIAM J. Sci. Comput.*, vol. 14, no. 6, pp. 1487–1503, 1993.

[28] I. Daubechies, "Orthonormal bases of compactly supported wavelets," *Commun. Pure Appl. Math.*, vol. 41, no. 7, pp. 909–996, 1988.

[29] H. Yang, S. Bukkapatnam, and R. Komanduri, "Nonlinear adaptive wavelet analysis of electrocardiogram signals," *Phys. Rev. E*, vol. 76, no. 2, 2007, Art. no. 026214.

[30] M. D. Cerqueira *et al.*, "Standardized myocardial segmentation and nomenclature for tomographic imaging of the heart a statement for healthcare professionals from the cardiac imaging committee of the council on clinical cardiology of the american heart association," *Circulation*, vol. 105, no. 4, pp. 539–542, 2002.

[31] A. L. Goldberger *et al.*, "PhysioBank, PhysioToolkit, and PhysioNet: Components of a new research resource for complex physiologic signals," *Circulation*, vol. 101, no. 23, pp. e215–e220, 2000.

Authors' photographs and biographies not available at the time of publication.